

Upconversion photoluminescence of Er-doped $Bi4Ti_3O_{12}$ ceramics enhanced by vacancy clusters revealed by positron annihilation spectroscopy

Huiru Cheng(程慧茹), Yuhuan Li(李钰环), Ziwen Pan(潘子文), Jiandang Liu(刘建党)†, and Bangjiao Ye(叶邦角)‡

Citation: Chin. Phys. B, 2024, 33 (**12**): 126102. DOI: 10.1088/1674-1056/ad84ca
Journal homepage: http://cpb.iphy.ac.cn; http://iopscience.iop.org/cpb

What follows is a list of articles you may be interested in

Effect of structural vacancies on lattice vibration, mechanical, electronic, and thermodynamic properties of Cr_5BSi_3

Tian-Hui Dong(董天慧), Xu-Dong Zhang(张旭东), Lin-Mei Yang(杨林梅), and Feng Wang(王峰)
Chin. Phys. B, 2022, 31 (**2**): 026101. DOI: 10.1088/1674-1056/ac11e2

Influence of helium on the evolution of irradiation-induced defects in tungsten: An object kinetic Monte Carlo simulation

Peng-Wei Hou(侯鹏伟), Yu-Hao Li(李宇浩), Zhong-Zhu Li(李中柱), Li-Fang Wang(王丽芳), Xingyu Gao(高兴誉), Hong-Bo Zhou(周洪波), Haifeng Song(宋海峰), and Guang-Hong Lu(吕广宏)
Chin. Phys. B, 2021, 30 (**8**): 086108. DOI: 10.1088/1674-1056/abf7ac

Effects of temperature and point defects on the stability of C15 Laves phase in iron: A molecular dynamics investigation

Hao Wang(王昊), Ning Gao(高宁), Guang-Hong Lü(吕广宏), Zhong-Wen Yao(姚仲文)
Chin. Phys. B, 2018, 27 (**6**): 066104. DOI: 10.1088/1674-1056/27/6/066104

Effect of size on momentum distribution of electrons around vacancies in NiO nanoparticles

Anjan Das, Atis Chandra Mandal, P. M. G. Nambissan
Chin. Phys. B, 2015, 24 (**4**): 046102. DOI: 10.1088/1674-1056/24/4/046102

Effect of size on momentum distribution of electrons around vacancies in NiO nanoparticles

Anjan Das, Atis Chandra Mandal, P. M. G. Nambissan
Chin. Phys. B, 2015, 24 (**4**): 046102. DOI: 10.1088/1674-1056/24/4/046102

Upconversion photoluminescence of Er-doped $Bi_4Ti_3O_{12}$ ceramics enhanced by vacancy clusters revealed by positron annihilation spectroscopy

Huiru Cheng(程慧茹), Yuhuan Li(李钰环), Ziwen Pan(潘子文),
Jiandang Liu(刘建党)[†], and Bangjiao Ye(叶邦角)[‡]

State Key Laboratory of Particle Detection and Electronics, University of Science and Technology of China, Hefei 230026, *China*

(Received 26 July 2024; revised manuscript received 11 September 2024; accepted manuscript online 9 October 2024)

Doping of rare earth elements into $Bi_4Ti_3O_{12}$ can significantly enhance the upconversion photoluminescence (UCPL) properties, but its structure–property relationship is still unclear. In this work, Er-doped bismuth titanate $Bi_{4-x}Er_xTi_3O_{12}$ ($x = 0$, 0.1, 0.2, 0.3, 0.4, 0.5) ceramics were synthesized via solid-state reaction method. The x-ray diffraction analysis confirmed the orthorhombic crystalline structure of the $Bi_{4-x}Er_xTi_3O_{12}$ ceramics without any secondary phases. Experiments and calculations of positron annihilation spectroscopy were carried out to characterize their defect structure. The comparison between the experimental and calculated lifetime revealed that vacancy clusters were the main defects in the ceramics. The increase of the intensity of the second positron lifetime component (I_2) of $Bi_{3.5}Er_{0.5}Ti_3O_{12}$ ceramics indicated the presence of a high concentration of vacancy clusters. The UCPL spectra showed the sudden enhanced UCPL performance in $Bi_{3.7}Er_{0.3}Ti_3O_{12}$ and $Bi_{3.5}Er_{0.5}Ti_3O_{12}$ ceramics, which were consistent with the variation of the second positron lifetime component (I_2). These results indicate that the enhanced UCPL properties are influenced not only by the concentrations of rare earth ions but also by the concentration of vacancy clusters present within the ceramics.

Keywords: bismuth layered structure, positron annihilation lifetime spectroscopy, upconversion photoluminescence, vacancy clusters

PACS: 61.72.jd, 78.70.Bj, 78.40.–q **DOI:** 10.1088/1674-1056/ad84ca

1. Introduction

The UCPL process is a nonlinear anti-Stokes phenomenon known for its ability to absorb two or more longer wavelength photons, typically near-infrared (NIR) or infrared (IR) light, and emit a shorter wavelength photon in the visible or ultraviolet spectrum.[1,2] This unique characteristic has garnered significant interest in rare-earth-doped oxide materials due to their promising applications in areas such as bioimaging, three-dimensional (3D) displays, solid-state lasers, and dispersive thermodynamics of localized carriers.[3–6] The UCPL materials consist of two essential components: the luminescent center, typically comprised of rare earth ions, and the matrix material, which provides a suitable crystal field for the luminescent center to facilitate the UCPL process.[7–9] In order to achieve high UCPL efficiency in the visible and mid-infrared spectral regions, the selection of appropriate matrix materials is crucial. Common upconversion matrix materials include fluorides, oxides, phosphates, and sulfides. Among these materials, Aurivillius-type bismuth layered structured ferroelectric (BLSF) materials are highly regarded for their excellent thermal stability, mechanical properties, ease of preparation, and eco-friendliness. BLSF materials belong to an important group of ferroelectric substances and are considered one of the most promising substrate materials for upconversion processes. The general formula of BLSF materials is $(Bi_2O_2)^{2+}(A_{m-1}B_mO_{3m-1})^{2-}$, where A is a mono-, di-, or trivalent ion or a mixture of them, B is a transition element suited for octahedral coordination (Ti^{4+}, Nb^{5+}, V^{5+}, Mo^{6+}, W^{6+}, *etc.*), and m is the number of octahedral layers in the perovskite slab, which can range from 1 to 6.[10–12] Bismuth titanate ($Bi_4Ti_3O_{12}$) is a typical Aurivillius-type bismuth layered ferroelectric material with $m = 3$, including $(Bi_2O_2)^{2+}$ layers and $(Bi_2Ti_3O_{10})^{2-}$ perovskite-like layers.

Rare earth ions, including Er^{3+}, Tm^{3+}, Ho^{3+}, Nd^{3+}, and Pr^{3+}, serve as the luminescent centers in conjunction with various matrix materials, leading to the emission of intense visible light upon excitation with IR light.[13,14] Among these rare earth ions, Er^{3+} stands out as the most efficient upconversion luminescent activator, owing to its ability to effectively absorb pump energy at 800 nm and 980 nm due to its substable energy levels $^4I_{9/2}$ and $^4I_{11/2}$.[13–15] Trivalent rare-earth ion dopants interaction with surrounding ions can cause the energy levels of the rare-earth ions to split and shift, while the matrix material itself exhibits lattice vibrations. If the frequency of lattice vibrations closely matches the excitation light frequency, more excitation light will be absorbed, enhancing its own vibration. And the excitation UCPL will be weakened.[16–18]

[†]Corresponding author. E-mail: liujd@ustc.edu.cn
[‡]Corresponding author. E-mail: bjye@ustc.edu.cn

© 2024 Chinese Physical Society and IOP Publishing Ltd

Good ferroelectric and UCPL properties have been obtained in Er-doped $Bi_4Ti_3O_{12}$ ceramics, but the correlation between defects and its UCPL characteristics remains insufficiently investigated. The UCPL properties of Er-doped ferroelectrics are closely related to the crystal field, which is influenced by both the crystal symmetry and the chemical environment of the matrix materials. The changes in the crystal microstructure of the matrix material can cause changes in the crystal field, which in turn affects the changes in the energy level of the activating ion and the improvement of the UCPL efficiency. However the direct experimental evidence validating the impact of vacancy defects on UCPL properties is scarce, primarily due to the absence of a suitable methodology for characterizing atomic-scale vacancy defects.[19]

Positron annihilation spectroscopy (PAS) stands out as a highly sensitive tool for examining and understanding atomic-scale defects in solids.[20,21] Positrons, due to their positive charge, exhibit a tendency to preferentially captured by vacancy defects in materials with lower electron density, enabling the selective identification of vacancy-type defects. This technique has been widely used to study vacancy defects in a variety of functional materials.[22,23] In this study, $Bi_4Ti_3O_{12}$ ceramics doped with different concentrations of Er^{3+} were synthesized by the solid-state reaction method. The defects within the ceramics were analyzed using positron annihilation lifetime spectroscopy (PALS). By combining with first principles theoretical calculations, the impact of defects on the UCPL properties of the samples was systematically explored.

2. Experiments

$Bi_{4-x}Er_xTi_3O_{12}$ ceramics compositions with varying Er^{3+} concentrations ($x = 0$, 0.1, 0.2, 0.3, 0.4, 0.5) were synthesized through a conventional solid-state reaction method. High-purity Bi_2O_3 (99.9%), TiO_2 (99.5%), and Er_2O_3 (99.9%) were used as the initial raw materials. The powders were carefully measured according to the stoichiometric formula and subsequently milled in an agate mortar for 2 hours using ethanol as a dispersing medium. These mixed oxides were then calcined at 850 °C for 3 hours in the air. Following calcination, the resulting powder was mixed with 5-wt% polyvinyl alcohol (PVA) binder. After a thorough mixing process, the dry powder was pressed into circular discs of approximately 1.0-mm thickness and 10.0-mm diameter using a hydraulic press. The pellets were then sintered in air at 1050 °C for 3 hours, with intermittent heat treatment at 600 °C for 2 hours to ensure complete burning out of the PVA binder. Finally, the samples were naturally cooled to room temperature.

The structural characteristics of the samples were investigated using x-ray diffraction (XRD) analysis with Cu $K\alpha$ radiation (SmartLab). The UCPL spectra were measured using a steady-state/lifetime spectrofluorometer (Fluorolog-3-Tau and Deltaflex) under 980-nm diode laser excitation at room temperature. Positron annihilation lifetime spectroscopy (PALS), as shown in Fig. 1, was used to analyze the variabilities of defect characteristics within these samples. Detection of the gamma rays was achieved using BaF_2 scintillators coupled with Hamamatsu H3378 photomultiplier tubes. A sandwich structure of ^{22}Na positron source with an activity level of 30 μCi was employed. The PALS has a time resolution of 200 ps and each spectrum contained approximately 6×10^6 coincidence counts. Yttria-stabilized zirconia (YSZ) samples were employed for source correction in the PALS experiments. All spectra were fitted using the LTv9 program.[24]

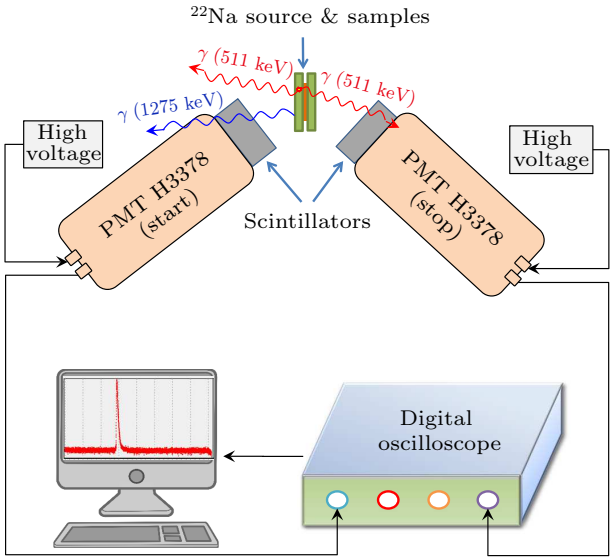


Fig. 1. Schematic diagram of the experimental setup of positron annihilation lifetime spectroscopy.

3. Results and discussion

3.1. Structural properties

The phase purity and crystallinity of the $Bi_{4-x}Er_xTi_3O_{12}$ ceramics were evaluated based on x-ray diffraction (XRD). Figure 2 shows the room temperature XRD patterns of the Er^{3+}-doped $Bi_{4-x}Er_xTi_3O_{12}$ series ceramics in the range of 20°–70°. The diffraction peaks in Fig. 2 align with those of the standard pattern (PDF card: No. 72-1019) for the orthorhombic structure, signifying the absence of secondary phases in the $Bi_{4-x}Er_xTi_3O_{12}$ samples. This confirms the successful fabrication of $Bi_{4-x}Er_xTi_3O_{12}$ with a single-phase structure via solid-state synthesis. The highest peak intensity corresponding to the (117) plane of $Bi_{4-x}Er_xTi_3O_{12}$ represents the BLSF with $m = 3$, which agrees with the former explanations that the strong intensity diffraction peak corresponds to the $(112m+1)$ plane for BLSF materials in the Aurivillius phase.[25] Notably, certain peaks like (028), (117), and (0014) exhibited significant changes in intensity with increasing Er^{3+} doping concentration, suggesting an influence of Er^{3+} doping on the lattice structure of the material. This effect is attributed to the smaller

ionic radius of Er^{3+} compared to Bi^{3+}, resulting in a slight shift of the (008) peak towards larger diffraction angles.

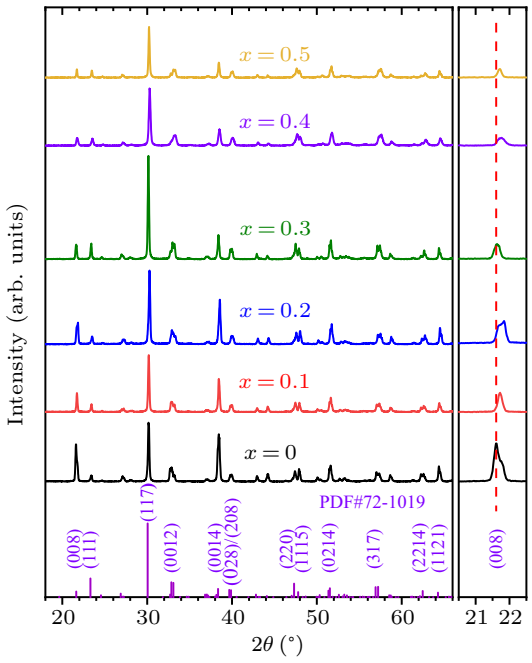


Fig. 2. XRD patterns of $Bi_{4-x}Er_xTi_3O_{12}$ ceramics with different Er contents.

The average grain size of the $Bi_{4-x}Er_xTi_3O_{12}$ ceramics are calculated by Scherrer's formula:

$$D = \frac{K\lambda}{\beta \cos\theta}, \tag{1}$$

where D is the average grain size, K is the shape factor (usually taken as 0.89), λ is taken as the x-ray wavelength of Cu $K\alpha$ radiation ($\lambda = 0.15418$ nm), β is the FWHM (full width at half maximum) of the XRD peak (every observed peak in the spectra was fitted with a Gaussian function), and θ is the Bragg angle. The impact of instrumental broadening on the FWHM has been considered.[26] The calculated grain sizes of the Er^{3+}-doped $Bi_{4-x}Er_xTi_3O_{12}$ samples are illustrated in Fig. 3. As the Er^{3+} content x increases, the grains exhibit random growth patterns. Among the series, $Bi_{3.5}Er_{0.5}Ti_3O_{12}$ exhibits the largest grain size.

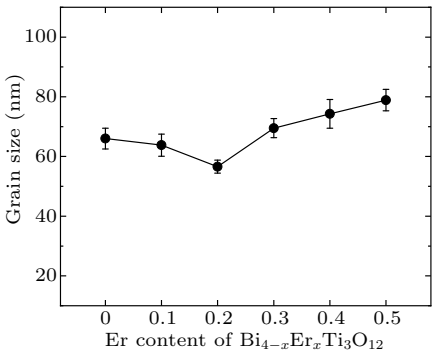


Fig. 3. The grain size of $Bi_{4-x}Er_xTi_3O_{12}$ ceramics calculated from XRD patterns.

3.2. PALS experimental and theoretical analysis

In order to obtain a more detailed microstructural analysis of $Bi_{4-x}Er_xTi_3O_{12}$, positron annihilation lifetime measurements were carried out. Utilizing the LTv9 program, the obtained spectra for all samples could be resolved into three components. The longest lifetime component τ_3 (longer than 1.5 ns) was the ortho-positronium annihilation lifetime formed at the surface or the interspace between the materials.[21] The measured positron lifetimes and their intensities are presented in Table 1. The average positron lifetime τ_{av} ($\tau_{av} = \tau_1 I_1 + \tau_2 I_2 + \tau_3 I_3$) of $Bi_{4-x}Er_xTi_3O_{12}$ ceramics were calculated.[27]

Table 1. Analysis results of positron annihilation lifetime spectra of $Bi_{4-x}Er_xTi_3O_{12}$ ceramics.

x	τ_1 (ps)	τ_2 (ps)	τ_3 (ns)	I_1 (%)	I_2 (%)	I_3 (%)	τ_{av} (ps)
0	213.6 ± 0.7	330.8 ± 1.2	2.3 ± 0.1	79.0 ± 0.6	20.3 ± 0.6	0.7 ± 0.1	251.9 ± 2.5
0.1	210.8 ± 0.5	347.0 ± 7.8	1.9 ± 0.1	78.9 ± 0.9	19.9 ± 0.9	1.3 ± 0.1	260.1 ± 11.1
0.2	209.2 ± 0.4	373.9 ± 2.3	2.3 ± 0.1	80.6 ± 0.1	18.0 ± 0.1	1.4 ± 0.1	266.5 ± 7.1
0.3	198.0 ± 2.1	322.6 ± 6.7	2.2 ± 0.1	76.7 ± 1.7	22.6 ± 1.7	0.7 ± 0.1	240.1 ± 7.0
0.4	201.4 ± 0.5	344.9 ± 5.4	2.0 ± 0.1	79.8 ± 0.7	19.2 ± 0.7	1.0 ± 0.1	247.8 ± 3.2
0.5	209.0 ± 0.6	393.4 ± 2.2	2.2 ± 0.1	72.2 ± 0.4	25.8 ± 0.4	2.0 ± 0.1	295.5 ± 2.1

As the Er-doped content increases, the slight variations in lifetime τ_1 with increasing Er-doped content reflect the structural perfectiveness of the $Bi_{4-x}Er_xTi_3O_{12}$ ceramics. The changes in the average positron lifetime, τ_{av}, are illustrated in Fig. 4(c), with the intensity of I_3 being negligible and thus disregarded in subsequent discussions. Both positron lifetimes τ_2 and τ_{av} follow a similar trend. The positron lifetimes τ_2, τ_{av}, and the intensity I_2 increase obviously at $x = 0.5$, as depicted in Fig. 4.

Notably, there is a lack of reports on the positron lifetime in $Bi_4Ti_3O_{12}$. With the aim of understanding our experimental results better, theoretical positron lifetimes in $Bi_4Ti_3O_{12}$ were calculated,[28] and the calculated results are presented in Table 2. The initial structure of the constructed bismuth titanate crystal comprised 76 atoms, including 16 Bi atoms, with a CODID of 1528445 and a space group of *Aba*2. To enable Er atom doping, the cell is expanded into a $1 \times 1 \times 5$ supercell. At a doping level of $x = 0.2$, the substitution involved replacing 4 Bi atoms with Er atoms in the desired proportion. Without considering the influence of the relative position of atoms, the calculated theoretical positron lifetimes are listed in Table 2. The data indicate that the bulk and vacancy-type positron lifetimes at different doping levels exhibit a similar trend, with a slight upward tendency. The lifetime associ-

ated with Ti-vacancy decreases with increasing doping concentration, while the lifetime linked to Bi-vacancy increases marginally with higher doping. Thus, it is believed that the doping concentration does not significantly alter the bulk and vacancy positron lifetimes in the samples. The calculated positron density distribution for the (010) plane is shown in Fig. 5. The Bi-vacancy and Ti-vacancy serve as effective trap centers for positrons due to their negatively charged nature, as demonstrated in Figs. 5(a) and 5(b). Additionally, the positron distribution around the Bi-vacancy center was more concentrated than that around the Ti-vacancy center, as shown in Fig. 5(c).

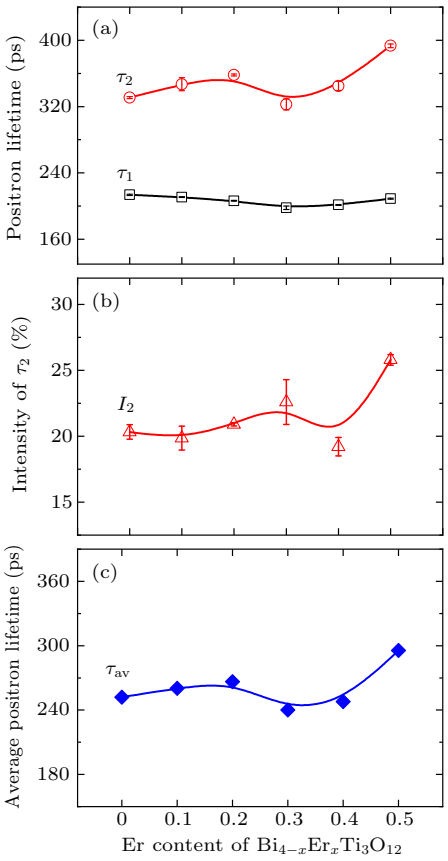


Fig. 4. Variation of positron lifetime (a) τ_1, τ_2, (b) I_2, and (c) τ_{av} in $Bi_{4-x}Er_xTi_3O_{12}$ with different Er contents.

Table 2. Calculated positron annihilation lifetime values (in units of ps) of different vacancy states in $Bi_{4-x}Er_xTi_3O_{12}$ ceramics.

x	Bulk	V_O	V_{Ti}	V_{Ti-Ti}	V_{Bi}	V_{Bi-Bi}
0	161.1	161.0	185.0	193.6	237.5	245.4
0.2	161.1	161.8	185.6	193.7	238.5	256.3
0.4	161.2	161.5	184.7	194.0	240.6	258.0
0.6	161.8	161.9	182.6	193.2	242.0	258.2
0.8	161.9	161.9	182.1	193.4	243.4	258.7

A comparison between the experimental and calculated data shows that the second lifetime component τ_2 significantly exceeded the calculated positron lifetimes in divacancies from Table 2. This discrepancy indicates that τ_2 is likely attributed to positron annihilation occurring within multi-vacancies or intricate vacancy clusters. In order to investigate defect variations further, positron lifetimes of certain vacancy complexes were computed and listed in Table 3. By examining the two positron lifetime components of Er-doped $Bi_{4-x}Er_xTi_3O_{12}$ ceramics, it appears that all positrons were completely trapped by defects. The first positron lifetime components τ_1, closely align with the calculated lifetimes associated with V_{Ti-O} given in Table 3 and V_{Ti-Ti} given in Table 2, indicating that τ_1 is likely attributed to positron annihilation in Ti-related divacancies. The second positron lifetime components τ_2 has a range from 322.6 ps to 393.4 ps in Table 1. Analysis of the calculated results in Table 3, it is evident that the cluster created by removing both two Bi and a Ti cation, along with one nearest oxygen neighbor, exhibits a lifetime of 326.2 ps. Furthermore, the removal of an additional neighboring oxygen from this complex led to a further increase in the lifetime, reaching 342 ps. This analysis supports the notion that τ_2 is associated with positron annihilation within vacancy clusters or grain boundaries.

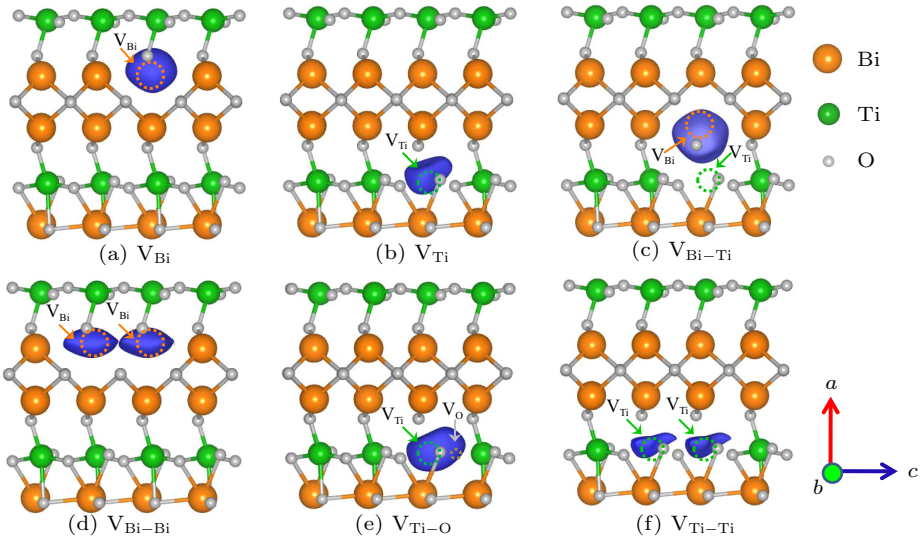


Fig. 5. Schematic representation of the positron density at (a) V_{Bi} monovacancy, (b) V_{Ti} monovacancy, (c) V_{Bi-Ti} divacancy, (d) V_{Bi-Bi} divacancy, (e) V_{Ti-O} divacancy, and (f) V_{Ti-Ti} divacancy in $Bi_4Ti_3O_{12}$.

Table 3. Calculated positron annihilation lifetime values of vacancy complexes in $Bi_4Ti_3O_{12}$.

Defect type	V_{Ti-O}	V_{Bi-Bi}	$V_{Bi-O-Ti}$	$V_{2Bi-O-Ti}$	$V_{2Bi-2O-Ti}$	V_{4Bi-2O}	V_{4Bi-3O}
Lifetime (ps)	220.1	245.4	284.8	326.2	342.0	375.0	437.8

The lifetime components τ_2 and τ_{av} reached a maximum at $x = 0.5$ ($Bi_{3.5}Er_{0.5}Ti_3O_{12}$) as shown in Figs. 4(a) and 4(c), indicating that $Bi_{3.5}Er_{0.5}Ti_3O_{12}$ sample possesses the largest defects among all samples. In addition, figure 4(b) illustrates a significant increase in the I_2 values for the $Bi_{3.5}Er_{0.5}Ti_3O_{12}$ samples, indicating a higher prevalence of vacancy clusters in these samples.

3.3. Upconversion photoluminescence properties

The UCPL spectra of the Er-doped $Bi_{4-x}Er_xTi_3O_{12}$ ceramics under 980-nm excitation at room temperature are shown in Fig. 6. The spectra of all the samples exhibit three distinct luminescent bands. These include two green bands with luminescence peaks at 528 nm and 548 nm, corresponding to the transitions $^2H_{11/2} \rightarrow {}^4I_{15/2}$ and $^4S_{3/2} \rightarrow {}^4I_{15/2}$ respectively, as well as a red band with a luminescence peak at 661 nm corresponding to the transition $^4F_{9/2} \rightarrow {}^4I_{15/2}$. The observed UC emission bands are consistent with previous reports on other Er^{3+} doped materials.[29,30] It is important to note that the luminescence of rare earth ions is primarily attributed to radiation transitions between energy levels. The lanthanide contraction of rare earth ions allows the 4f orbitals to be well shielded from external crystal field environments, thereby remaining largely unaffected.[31] Consequently, changing the doping concentration of Er^{3+} ions will not shift the position of the emission peak, but only change the intensity of the emission peak. The spectra of the Er^{3+} transitions represent some discrete set of narrow lines, suggesting that the Er^{3+} occupies the crystalline site, which is also consistent with the experimental results of XRD.

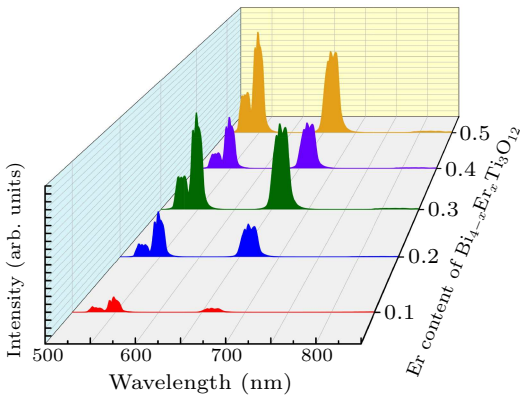


Fig. 6. UC emission spectra of $Bi_{4-x}Er_xTi_3O_{12}$ ceramics with varying Er contents under 980-nm excitation.

For the UCPL process, the UCPL mechanism must be discussed based on the energy level diagram of Er^{3+}. Figure 7 exhibits the energy level diagram of Er^{3+} ions as well as the probable UCPL mechanisms accounting for the green and red emissions. The UCPL process of Er^{3+} typically involves six main steps: ground state absorption (GSA), excited state absorption (ESA), energy transfer (ET), multiphonon relaxation (MPR), cross relaxation (CR), and emission. When Er^{3+}-doped samples are excited with 980-nm laser, Er^{3+} ions at the ground level $^4I_{15/2}$ absorb photons and transition to the $^4I_{11/2}$ level through GSA. Subsequently, some excited Er^{3+} ions at the $^4I_{11/2}$ level can absorb one more photon, elevating them to the $^4F_{7/2}$ level via the ESA process. In addition, two excited state Er^{3+} ions at $^4I_{11/2}$ can interact with each other through ($^4I_{11/2}$ + $^4I_{11/2} \rightarrow {}^4I_{15/2}$ + $^4F_{7/2}$) ET process. Both of the above processes can amass the ion numbers of the $^4F_{7/2}$ level. Then, the population Er^{3+} ions at the $^4F_{7/2}$ level will decay non-radiatively to the $^2H_{11/2}$, $^4S_{3/2}$, and $^4F_{9/2}$ levels by the MPR process, resulting in the emission of green $^2H_{11/2}/{}^4S_{3/2} \rightarrow {}^4I_{15/2}$ and red $^4F_{9/2} \rightarrow {}^4I_{15/2}$ bands.[32] The mechanism involved in the UC emission in the green bands can be expressed as

$$^4F_{7/2} \rightarrow {}^2H_{11/2}, \quad {}^4S_{3/2} \rightarrow {}^4I_{15/2}. \tag{2}$$

For red emission, the Er^{3+} ions at the $^4F_{9/2}$ level can be populated by four possible ways and represented as

$$^4S_{3/2} \rightarrow {}^4F_{9/2} \rightarrow {}^4I_{15/2}, \tag{3}$$

$$^4I_{13/2} + \text{ESA} \rightarrow {}^4F_{9/2} \rightarrow {}^4I_{15/2}, \tag{4}$$

$$^4I_{13/2} + {}^4I_{11/2} \rightarrow {}^4F_{9/2} \rightarrow {}^4I_{15/2}, \tag{5}$$

$$^4F_{7/2} + {}^4I_{11/2} \rightarrow {}^4F_{9/2} \rightarrow {}^4I_{15/2}. \tag{6}$$

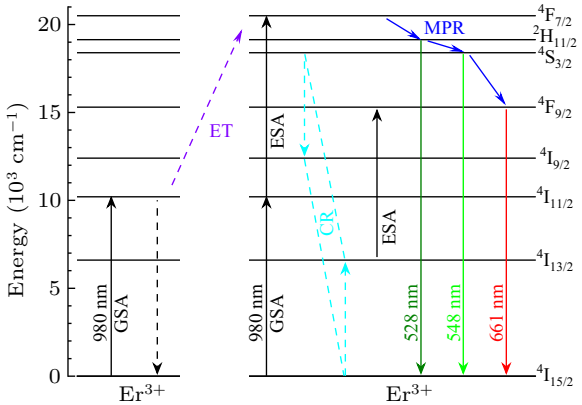


Fig. 7. Schematic diagram of the UCPL mechanism of Er^{3+} ions.

In Fig. 6, it is evident that at lower Er^{3+} doping concentrations, the UCPL efficiency is notably weak when excited under 980-nm lasers, causing the corresponding GSA, ESA, and ET processes limited and the emissions are weak. Figure 8 shows the UCPL peak intensities as a function of the Er^{3+} contents. As shown in Fig. 8(a), the UCPL peak

intensities of 528 nm, 548 nm, and 661 nm increase with increasing the concentration of Er^{3+} ($x \leq 0.3$). Afterward, a sudden decline in emission intensity (x) is considered to be due to the intensified concentration quenching effects. At high concentrations of activated Er^{3+} ions, the distances between centers fall below a critical threshold, leading to cascading energy transfers, or energy migration, from one center to another until reaching a quenching center, eventually resulting in luminescence quenching. Nevertheless, the UCPL peak intensities start to increase again with the increasing Er^{3+} content. In general, the UCPL intensity is dependent on the structural distortion and the symmetric crystal field is unfavorable for the UC emission because the f–f transition is originally prohibited under high spherical symmetry. The rise in crystal structure defects altered the microstructural environment in which Er^{3+} was located, thereby modifying the symmetry of the crystal field. Combined with the analysis of positron annihilation results, high concentration vacancy clusters exist in $Bi_{3.5}Er_{0.5}Ti_3O_{12}$ ($x = 0.5$), leading to increase in crystal lattice distortion. The ratio $I_{548\ nm}/I_{528\ nm}$ experiences a sharp decrease at $x = 0.3$ and $x = 0.5$ as presented in Fig. 8(b), possibly indicating a reduction in the emission intensity of $^4S_{3/2} \rightarrow {}^4I_{15/2}$ through non-radiative relaxation to the lower $^4F_{9/2}$ state. Furthermore, figure 8(c) demonstrates a rapid increase in the $I_{661\ nm}/I_{548\ nm}$ ratio, possibly attributed to CR processes from the $^4F_{7/2}$ state to the red-emitting $^4F_{9/2}$ state

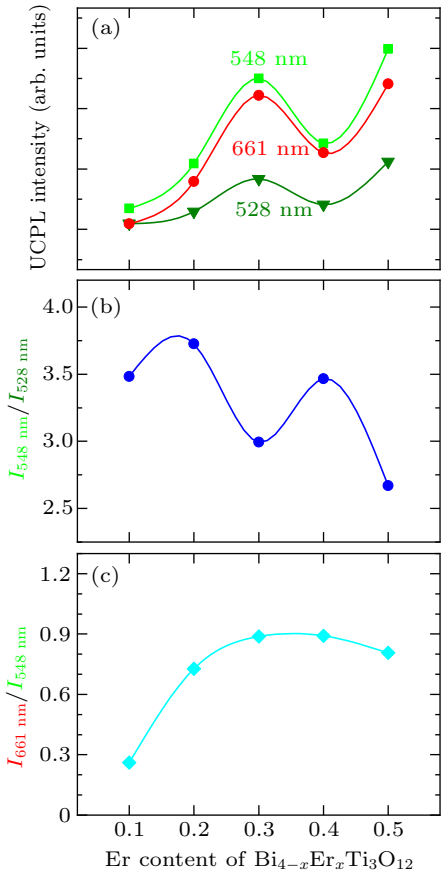


Fig. 8. Comparison of the (a) UCPL peak intensities, (b) $I_{548\ nm}/I_{528\ nm}$, (c) $I_{661\ nm}/I_{548\ nm}$ of $Bi_{4-x}Er_xTi_3O_{12}$ ceramics as a function of the Er contents.

($^4F_{7/2} + {}^4I_{11/2} \rightarrow 2{}^4F_{9/2}$), facilitated by a decrease in the distance between Er^{3+} ions. Within the Er^{3+} concentration range from $x = 0.3$ to $x = 0.5$, the $I_{661\ nm}/I_{548\ nm}$ ratio remains relatively stable. The interionic CR rate is inversely proportional to the sixth square of the distance between ions reported in the literature.[33] When $x \geq 0.3$, enhanced interactions and CR processes ($^4S_{3/2} + {}^4I_{15/2} \rightarrow {}^4I_{9/2} + {}^4I_{13/2}$, $^4F_{7/2} + {}^4I_{11/2} \rightarrow 2{}^4F_{9/2}$, $^4I_{15/2} + {}^4I_{9/2} \rightarrow 2{}^4I_{13/2}$) between Er^{3+} play a dominant role.

The UCPL intensity has a peak at $x = 0.3$. As the Er content increases, the concentration of vacancy clusters reaches a maximum, coinciding with the maximum UCPL intensity. This suggests that the concentration of Er^{3+} as active ions predominantly influences UCPL intensity for $x \leq 0.3$. When $x > 0.3$, a rapid decrease in UCPL intensity is observed along with an enhanced interaction between Er^{3+} ions. At $x = 0.5$, vacancy-type defects mitigate concentration quenching effects and subsequently contribute to a decrease in UCPL decline. The grain size of $Bi_{3.5}Er_{0.5}Ti_3O_{12}$ has a maximum value, indicating that grain size may indeed play a role in modulating UCPL intensity. High concentration vacancy clusters reduced the probability of concentration quenching, resulting in a significant increase in the UCPL intensity.

4. Conclusion

In summary, $Bi_{4-x}Er_xTi_3O_{12}$ ($x = 0$, 0.1, 0.2, 0.3, 0.4, 0.5) ceramics were synthesized by solid-state reaction method. The doping of Er^{3+} did not induce any phase changes in the $Bi_{4-x}Er_xTi_3O_{12}$ ceramics. A strong UCPL was observed in the Er-doped $Bi_4Ti_3O_{12}$ ceramics. The impact of rare earth ion concentration was the primary factor influencing UCPL intensity until $x = 0.3$, beyond which rare earth ions concentration saturation resulted in concentration quenching. Thus, higher concentrations of rare earth ions directly affected the abundance and size of defects in the samples, thereby influencing UCPL intensity variations. The results show a clear correlation between the UCPL behavior and the defects distribution, which gives an important insight into the role of vacancies in UCPL properties. This suggests a way to enhance UCPL properties by controlling defect concentrations.

Acknowledgements

Project supported by the National Key Research and Development Program of China (Grant No. 2019YFA0210000) and the National Natural Science Foundation of China (Grant No. 12175232).

References

[1] Auzel F 2004 *Chem. Rev.* **104** 139
[2] Wei T, Jia B, Shen L H, *et al.* 2021 *Acta. Mater.* **205** 116557
[3] Ma Y, Ji Y, You M, *et al.* 2016 *Acta. Biomater.* **42** 199
[4] Huang X, Guo Q, Kang S, *et al.* 2020 *ACS Nano.* **14** 3150
[5] Pant A, Xia X, Davis E J, *et al.* 2020 *Nat. Commun.* **11** 3235
[6] Su Z and Xu S 2017 *Sci. Rep.* **7** 13

[7] Lojpur V, Nikolić G and Dramićanin M D 2014 *J. Appl. Phys.* **115** 203106
[8] Feng Y S, Li Z, Li Q Q, *et al*. 2021 *Light. Sci. Appl.* **10** 105
[9] Wen S H, Zhou J J, Zheng K Z, *et al*. 2018 *Nat. Commun.* **9** 2415
[10] Zhang M, Xu X, Ahmed S, *et al*. 2022 *Acta. Mater.* **229** 117815
[11] Zhang Q, Shi Y, Shi X, *et al*. 2022 *Appl. Catal. B.* **302** 120876
[12] Gupta P, Mahapatra P and Choudhary R 2021 *J. Alloys Compd.* **863** 158457
[13] Wang X, Wang Y, Gao M, *et al*. 2020 *Appl. Catal. B.* **270** 118876
[14] Yin D G, Liu Y M, Tang J X, *et al*. 2020 *Light. Sci. Appl.* **9** 184
[15] Bokolia R, Thakur O, Rai V K, *et al*. 2015 *Ceram. Int.* **41** 6055
[16] An R, Liang Y, Deng R P, *et al*. 2022 *Light. Sci. Appl.* **11** 217
[17] Fu X, Fu S, Lu Q, *et al*. 2022 *Nat. Commun.* **13** 4741
[18] Liao J S, Wang M H, Lin F L, *et al*. 2022 *Nat. Commun.* **13** 2090
[19] Huang Y and Luo L 2017 *J. Alloys Compd.* **706** 312
[20] Krause-Rehberg R and Leipner H 1999 *Positron Annihilation in Semiconductors: Defect Studies* Vol. 127 (Springer Science & Business Median)
[21] Tuomisto F and Makkonen I 2013 *Rev. Mod. Phys.* **85** 1583
[22] Keeble D J, Singh S, Mackie R A, *et al*. 2007 *Phys. Rev. B.* **76** 144109
[23] Yan F, Liu Z, Chen J, *et al*. 2022 *Ceram. Int.* **48** 33135
[24] Kansy J 1996 *Nucl. Instrum. Methods Phys. Res. Sect. A* **374** 235
[25] Wang D, Xu Y, Shi Y, *et al*. 2019 *J. Am. Ceram. Soc.* **103** 266
[26] Sengar P, García-Tapia K, Can-Uc B, *et al*. 2019 *J. Appl. Phys.* **126** 083107
[27] Ali S I, Das A, Agrawal A, *et al*. 2021 *Chin. Phys. B* **30** 026103
[28] Zhang W S, Gu B C, Han X X, *et al*. 2015 *Chin. Phys. B* **24** 107804
[29] Pavani K, Kumar J S, Srikanth K, *et al*. 2017 *Sci. Rep.* **7** 17646
[30] Krishnan R, Nair G B, Menon S G, *et al*. 2021 *J. Alloys Compd.* **878** 160386
[31] Dong H, Sun L D and Yan C H 2021 *J. Am. Chem. Soc.* **143** 20546
[32] Xue S D, Deng H, Xie Q X, *et al*. 2019 *Nanoscale* **11** 16928
[33] Tarelho L V G, Gomes L and Ranieri I M 1997 *Phys. Rev. B* **56** 14344